Sparse Doppler Sensing Based on Nested Arrays

Regev Cohen, *Student, IEEE,* Yonina C. Eldar, *Fellow, IEEE*

Abstract—Spectral Doppler ultrasound imaging allows visualizing blood flow by estimating its velocity distribution over time. Duplex ultrasound is a modality in which an ultrasound system is used for displaying simultaneously both B-mode images and spectral Doppler data. In B-mode imaging short wide-band pulses are used to achieve sufficient spatial resolution in the images. In contrast, for Doppler imaging, narrow-band pulses are preferred in order to attain increased spectral resolution. Thus, the acquisition time must be shared between the two sequences. In this work, we propose a non-uniform slow-time transmission scheme for spectral Doppler, based on nested arrays, which reduces the number of pulses needed for accurate spectrum recovery. We derive the minimal number of Doppler emissions needed, using this approach, for perfect reconstruction of the blood spectrum in a noise-free environment. Next, we provide two spectrum recovery techniques which achieve this minimal number. The first method performs efficient recovery based on the fast Fourier transform. The second allows for continuous recovery of the Doppler frequencies, thus avoiding off-grid error leakage, at the expense of increased complexity. The performance of the techniques is evaluated using realistic Field II simulations as well as in vivo measurements, producing accurate spectrograms of the blood velocities using a significantly reduced number of transmissions. The time gained, where no Doppler pulses are sent, can be used to enable the display of both blood velocities and high quality B-mode images at a high frame rate.

Index Terms—Medical Ultrasound, Spectral Estimation, Nested Arrays, Blood Velocity Estimation, Blood Doppler

I. INTRODUCTION

SPECTRAL Doppler in medical ultrasound is a non-invasive imaging modality commonly used for quantitative estimation of blood velocity. The data for velocity estimation is acquired by insonifying the medium with a train of narrow-band ultrasound pulses along a desired direction at a constant pulse repetition frequency (PRF). The backscattered signals are then sampled and focused along the chosen direction using dynamic focusing. Assembling the samples associated with a specific depth of interest from all received signals forms the so-called slow-time signal with a center frequency proportional to the axial blood velocity.

For a single blood cell with axial velocity v_z, the slow-time signal has a center frequency equal to [1]

$$f_{\mathrm{D}} = -\frac{2v_z}{c}f_0 \qquad (1)$$

where f_0 is the center frequency of the transmitted signal and c is the speed of sound. In reality, there is a distribution of blood scatterers within each resolution cell of the ultrasound system. The blood velocity distribution is estimated by reconstructing the power spectral density (PSD) of the slow-time signal. Displaying spectral analysis results over time on a pulsed Doppler

spectrogram (also referred to as pulsed wave spectrogram), visualizes the evolution of the blood velocity distribution as a function of time. The time needed for each velocity estimation is the coherent processing interval (CPI), which is equal to the number of transmitted pulses P divided by the PRF. As the number of transmitted pulses per unit time is limited by the speed of sound and the desired depth being examined, there is an inherent trade off between spectral and temporal resolution.

In modern commercial ultrasound systems, the spectrogram is typically estimated using Welch's method [2], [3], a modified averaged periodogram based on the fast Fourier transform (FFT). However, this approach suffers from high leakage due to high sidelobes and/or low resolution. Since the resolution in Doppler frequency is governed by P, it requires a large number of consecutive transmissions to be used for each velocity estimate.

In addition to Doppler measurements, simultaneous high frame rate B-mode images are required to allow the physician to navigate, select the region in which the blood velocity is estimated and to examine anatomical structures surrounding the vessel. However, two distinct pulses are used for the two modes, B-mode and Doppler. In particular, for B-mode imaging short wide-band pulses with high carrier frequency are transmitted to increase resolution. Whereas, for Doppler imaging, narrow-band pulses with low center frequency are preferred in order to improve penetration depth and increase the precision of the velocity estimate. Moreover, the B-mode and Doppler pulses may be transmitted in different directions. Consequently, the acquisition time must be shared between the two imaging modalities.

In conventional imaging, an interleaved B-mode/Doppler sequence is used where every B-mode transmission is followed by a Doppler transmission. This halves the PRF, resulting in reduction of the maximal velocity that can be detected by a factor of two, according to the Nyquist theorem. An alternative common approach is to regularly interrupt the Doppler sequence for a block of B-mode transmissions. However, this results in holes in the blood velocity spectrogram. These limitations raise the need for developing improved techniques for blood spectrum estimation using considerably fewer Doppler transmissions.

To circumvent these problems Kristoffersen and Angelsen [4] proposed to fill in the Doppler gaps with a synthetic signal, generated based on the Doppler signal measured immediately prior to the B-mode interrupt. Klebaek et al. [5] proposed the use of neural networks for predicting the evolution of the mean and variance of the Doppler signal in the gaps. However, both methods are based on the assumption that the blood flow is constant or predictable which is not true in case of abrupt changes, leading to inaccurate velocity estimation. A correlation-based method for spectral estimation from sparse

data sets was proposed in [6], allowing for random Doppler transmission schemes, but it exhibits aliasing when using few Doppler emissions. This work was further investigated in [7], which proposed a technique for reconstructing the missing Doppler samples, due to B-mode transmissions, using filter banks. This method, however, reduces the velocity range in proportion to the number of missing Doppler samples.

Two data-adaptive velocity estimators for periodically gapped data, called BPG-Capon and BPG-APES, were suggested in [8], [9]. These methods are restricted to the case of periodically gapped sampling of Doppler emissions and have been shown to achieve a limited reduction of 34% in the number of transmissions. For arbitrary Doppler subsampling patterns, two iterative methods termed BSLIM and BIAA were presented in [10], [11]. However, they exhibit high computational load and require the use of regression filters for clutter removal, which may degrade the quality of the spectrum estimate by producing spurious frequency components [12].

Several works apply compress sensing (CS) [13] techniques to spectral Doppler using random slow-time samples. Zobly et al. apply basis pursuit (BP) in [14] and a multiple measurement vector (MMV) technique in [15] to recover the Doppler signal. However, the authors do not state the domain (dictionary) in which the signal is sparse. Furthermore, the resultant spectrograms exhibit artifacts. Assuming the Doppler signal is sparse under the Fourier transform or in the wave atom domain [16], Richy et al. propose [17], [18] decomposing the Doppler signal into several equal segments and applying CS recovery on each segment. However, this work does not consider the case of moderately or non sparse signals. Moreover, the reduction in the number of Doppler transmissions is limited to 60% using this method. An extension is presented in [19], which proposed to reconstruct the Doppler signal using block sparse Bayesian learning (BSBL) [20], [21]. However, the authors assume that the Doppler samples are temporally correlated and severe aliasing appears in their recovered spectra at high subsampling rates. In addition, the average computation time per segment using this technique is high, making it impractical for real-time implementation.

In addition to the computational complexity and recovery artifacts in the methods above, none of these works present an analysis of the minimal number of Doppler emissions ensuring adequate reconstruction of the blood spectrum, using their techniques.

The main contribution of this paper is twofold. First, adopting recent work on nested arrays [22], [23] in the fields of multiple-input multiple-output (MIMO) radar systems and direction of arrival (DOA) estimation, we present a non-uniform transmission scheme for spectral Doppler. Our theoretical approach does not assume the Doppler signal is sparse or its entries are correlated, nor that the blood flow is predictable. An analysis is performed, deriving the minimal number of Doppler emissions required using the nested approach. We show that the number of transmissions allowing for perfect reconstruction of the spectrum in a noise-free setting is proportional to the square root of the observation window length. Second, we propose two spectrum recovery techniques that achieve this minimal number of transmitted pulses. The first method assumes the Doppler frequencies lie on the Nyquist grid and recovers the spectrum using FFT. This technique exhibits enhanced resolution compared with Welch's method, and similar low complexity, making it suitable for real-time application. The second approach performs continuous recovery, thus preventing spectral leakage stemming from off-grid errors, at the expense of increased complexity. The performance of the techniques is validated using realistic Field II simulation data [24], [25] and in vivo data, showing that blood velocities can be accurately estimated from a reduced number of emissions.

The rest of the paper is organized as follows. In Section II, we review the Doppler signal model and formulate our problem. Section III describes the autocorrelation of the Doppler signal and introduces the proposed sparse slow-time sampling scheme. We then derive the minimal number of Doppler transmissions required using this emission pattern. In Section IV, we present discrete and continuous recovery techniques that achieve this minimal number. Alternative sparse transmission schemes are discussed in Section V. We evaluate the performance of the proposed algorithms in Section VI and compare them with existing state-of-the-art techniques. Finally, Section VII concludes the paper.

Throughput the paper we use the following notation. Scalars are denoted by lowercase letters (a), vectors by boldface lowercase letters $(\mathbf{a})$, matrices by boldface capital letters $(\mathbf{A})$ and sets are given by calligraphic font (e.g., $\mathcal{A}$). The (i, j)th element of $\mathbf{A}$ is denoted by $\mathbf{A}(i, j)$, $\mathbf{a}_l$ is the lth column of $\mathbf{A}$ and $\mathbf{a}(l)$ represents the lth element of $\mathbf{a}$. The notations $(\cdot)^T, (\cdot)^*$ and $(\cdot)^H$ indicate the transpose, conjugate and Hermitian operations, respectively. The vectorization of a matrix $\mathbf{A}$ into a column stack is given by $\text{vec}(\mathbf{A})$. For a positive integer P, $d|P$ implies that d is a divisor of P with $1 < d < P$.

II. DOPPLER MODEL AND PROBLEM FORMULATION

A. Doppler Model

A standard ultrasound system in spectral Doppler mode transmits a pulse train

$$s_{tx}(t) = \sum_{p=0}^{P-1} h(t - pT), \qquad 0 \le t \le PT, \qquad (2)$$

consisting of P equally spaced pulses $h(t)$. The pulse repetition interval (PRI) is T, and its reciprocal $f_{\text{prf}} = 1/T$ is the PRF. The entire span of the signal in (2) is called the CPI. The pulse $h(t)$ is a sinusoid defined as

$$h(t) = \sin(2\pi f_0 t), \quad 0 \le t \le T_{\max}, \qquad (3)$$

where f_0 is the center frequency of the signal and $T_{\max} < T$ is the pulse duration, determined by the desired axial resolution.

Consider a single blood scatterer. The pulses reflect off the scatterer and propagate back to the transducer. The noise-free received signal can be modeled as

$$s(t) = \sum_{p=0}^{P-1} \alpha \sin\left(2\pi f_0\left(t - pT - \frac{2d_p}{c}\right)\right), \qquad (4)$$

where p is the emission number, c is the sound wave propagation speed, α is the amplitude related to blood scatterer reflectivity and d_p is its depth at the time of the pth transmission. For mathematical convenience, we express $s(t)$ as a sum of single frames

$$s(t) = \sum_{p=0}^{P-1} s_p(t), \qquad (5)$$

where

$$s_p(t) = \alpha \sin\left(2\pi f_0\left(t - pT - \frac{2d_p}{c}\right)\right). \qquad (6)$$

The blood scatterer movement along the beam direction during P consecutive transmissions is given by

$$d_p = d_0 + v \cdot pT, \qquad 0 \le p \le P-1, \qquad (7)$$

where d_0 is the initial depth of the blood scatterer and v is its axial velocity. Substituting (7) into (6), we get

$$s_p(t) = \alpha \sin\left(2\pi f_0\left(t - pT - \frac{2d_0}{c} - \frac{2v}{c}pT\right)\right). \qquad (8)$$

Each frame is then aligned $\tilde{s}_p(t) = s_p(t + pT)$ and sampled at rate f_s, determined by the desired spatial axial resolution. This yields a 2D discrete signal

$$s[k,p] = \tilde{s}_p\left(\frac{k}{f_s}\right) = \alpha \sin\left(2\pi f_0\left(\frac{k}{f_s} - \frac{2d_0}{c} - \frac{2v}{c}pT\right)\right), \qquad (9)$$

where k is the sample index associated with depth.

The samples (9) form a 2D measurement matrix $\mathbf{S} \in \mathbb{C}^{K \times P}$ where $\mathbf{S}(k,p) = s[k,p]$. For a fixed pulse number p, the samples along the row dimension of $\mathbf{S}$ are referred to as fast-time samples and are related to the pth pulse transmission. Each fast-time sample corresponds to a different depth k of the scanned medium. For a given k, the samples along the column dimension of $\mathbf{S}$ are referred to as slow-time samples and are associated with the same depth, one sample per pulse emission.

Following (9), the analytical signal is generated to give the in-phase and quadrature components

$$x[k,p] = s[k,p] + j\mathcal{H}_k\{s[k,p]\} =$$
$$= \alpha \exp\left(2\pi j f_0\left(\frac{k}{f_s} - \frac{2d_0}{c} - \frac{2v}{c}pT\right)\right), \qquad (10)$$

where $\mathcal{H}_k\{\cdot\}$ is the discrete Hilbert transform in the fast-time direction. Since f_0/f_s is known, we demodulate the signal $x[k,p]$, resulting in

$$y[k,p] = \alpha \exp\left(-2\pi j f_0\left(\frac{2d_0}{c} + \frac{2v}{c}pT\right)\right). \qquad (11)$$

Define the complex amplitude $\tilde{\alpha} = \alpha \exp(-j\frac{4\pi d_0}{c}f_0)$ and denote the Doppler frequency by

$$f \triangleq -\frac{2v}{c}f_0. \qquad (12)$$

Then, we can represent the signal given in (11) as

$$y[k,p] = \tilde{\alpha} \exp\left(2\pi j f pT\right). \qquad (13)$$

Consider a specific depth k. The measured signal in (13) can be viewed as a realization of a continuous-time wide-sense stationary (WSS), comprises a zero-mean complex amplitude and a time invariant velocity

$$y_k(t) = \tilde{\alpha} \exp(2\pi j f t), \qquad (14)$$

which is sampled at time $t = pT$ ($0 \le p \le P - 1$), namely, at a sampling rate of f_{prf}. Decreasing the sampling interval T increases the maximal velocity that can be recovered according to the Nyquist theorem, however, there is a trade-off since it limits the maximal depth being examined. In addition, the spectral resolution is governed by P, motivating the desire to increase the number of transmissions as long as they are limited to be within the time in which the velocity is assumed to be constant.

In the general case, each resolution cell of the ultrasound imaging system contains a distribution of blood scatterers. Consequently, the measured signal consists of several spectra stemming from $M > 1$ unknown velocities. Taking the latter into account, we extend the signal model written in (13) to

$$y[k,p] = \sum_{m=1}^{M} \alpha_m \exp(2\pi j f_m pT), \qquad 0 \le p \le P - 1. \quad (15)$$

Therefore, the received signal is composed of M components where the mth component is defined by two parameters: a Doppler frequency f_m, proportional to an axial velocity v_m; and a complex random amplitude α_m, related to the number of blood cells moving at an axial velocity v_m and their positions. The Doppler frequencies $\{f_m\}_{m=1}^M$ are assumed to lie in the unambiguous frequency domain, that is $|f_m| \le \frac{1}{2T} = \frac{1}{2}f_{\text{prf}}$ for all $1 \le m \le M$.

Assembling the slow-time samples $y[k,p]$ for P consecutive transmissions into a vector we obtain

$$\mathbf{y}[k] = \mathbf{A}\boldsymbol{\alpha}, \qquad (16)$$

where $\mathbf{y}[k] = [y[k,0], y[k,1], ..., y[k,P-1]]^T \in \mathbb{C}^{P \times 1}$ is the slow-time vector, the vector $\boldsymbol{\alpha} \in \mathbb{C}^{M \times 1}$ consists of M amplitudes $\{\alpha_m\}_{m=1}^M$ and the matrix $\mathbf{A} \in \mathbb{C}^{P \times M}$ is a Vandermonde matrix, whose entries are given by $\mathbf{A}(p,m) = \exp(2\pi j f_m pT)$.

Based on the model (16), the goal is to recover the frequency components $\{f_m\}_{m=1}^M$ which form the matrix $\mathbf{A}$ and to estimate the variances $\{\sigma_m^2\}_{m=1}^M$ of the random vector $\boldsymbol{\alpha}$, i.e., the power spectrum.

B. Standard Processing

In standard Doppler processing [1], [2], the Doppler frequencies are assumed to lie on the Nyquist grid, that is $f_m T = i_m/P$, where i_m is an integer in the range $0 \le i_m \le P - 1$. Using this assumption, (16) can be rewritten with $\mathbf{A} = \mathbf{F}^H$ as

$$\mathbf{y}[k] = \mathbf{F}^H \boldsymbol{\alpha}, \qquad (17)$$

where $\mathbf{F} \in \mathbb{C}^{P \times P}$ is the FFT matrix. This implies that $\boldsymbol{\alpha}$ is a vector of length P with M non-zero values $\{\alpha_m\}_{m=1}^M$ at indices $\{i_m\}_{m=1}^M$. Consequently, the power spectrum, to be recovered, is defined as a vector $\mathbf{p} \in \mathbb{R}^{P \times 1}$ with a non-zero value σ_m^2 at index i_m.

Assuming we have enough snapshots of the slow-time vector $\mathbf{y}[k]$, a conventional estimate of the power spectrum is given by

$$\hat{\mathbf{p}}_{\text{standard}} = \frac{1}{K} \sum_{k=1}^{K} |\mathbf{F}\mathbf{y}[k]|^2, \qquad (18)$$

where the squared magnitude is computed element-wise. In this case, the spectral resolution is equal to $2\pi/PT$, where P is chosen large enough to attain sufficient resolution.

C. Problem Formulation

In this work, we wish to recover the power spectrum $\mathbf{p}$ with improved spectral resolution while significantly reducing the number of transmitted Doppler pulses.

For an observation window of size P, we propose a new transmission strategy in which only $N < P$ pulses are sent with non-uniform time steps between them over the entire CPI. We show that the power spectrum can be fully reconstructed with a resolution of $2\pi/(2P-1)T$ at the same complexity of standard processing. Note that we do not recover the slow-time signal but only its power spectrum. We prove that $N = 2\sqrt{P} - 1$ is the minimal number of transmissions enabling perfect reconstruction of the spectrum in a noise-free environment using our approach, and present recovery techniques that achieve this number.

Using our techniques, we allow periods of time where no Doppler pulse is sent, which can be exploited for B-mode transmission sequences. Consequently, the same CPI may be used to achieve Doppler velocity estimates and high quality B-mode images at a high frame rate.

III. Nested Slow-Time Sampling

In this section, we present a non-uniform Doppler transmission scheme from which the blood spectrum may be recovered with improved resolution, in comparison to standard processing. We first extend the signal model (16) by deriving an expression for the signal autocorrelation function.

A. Correlation Domain

Consider the model given by (16) and define the autocorrelation matrices $\mathbf{R}_{\mathbf{y}} = \mathbb{E}[\mathbf{y}\mathbf{y}^H] \in \mathbb{C}^{P \times P}$ and $\mathbf{R}_{\boldsymbol{\alpha}} = \mathbb{E}[\boldsymbol{\alpha}\boldsymbol{\alpha}^H] \in \mathbb{C}^{M \times M}$. Then,

$$\mathbf{R}_{\mathbf{y}} = \mathbf{A}\mathbf{R}_{\boldsymbol{\alpha}}\mathbf{A}^H. \qquad (19)$$

We further assume that the amplitudes are statistically uncorrelated with unknown variances such that

$$\mathbb{E}[\alpha_m \alpha_n^*] = \sigma_m^2 \delta[n - m], \qquad (20)$$

where $\delta[\cdot]$ is the Kronecker delta. Under this assumption, the matrix $\mathbf{R}_{\boldsymbol{\alpha}}$ is a diagonal matrix with $\mathbf{R}_{\boldsymbol{\alpha}}(m, m) = \sigma_m^2$. Denoting the diagonal of $\mathbf{R}_{\boldsymbol{\alpha}}$ by $\mathbf{p} \in \mathbb{R}^{M \times 1}$, it follows that

$$\mathbf{r} \triangleq \text{vec}(\mathbf{R}_{\mathbf{y}}) = (\mathbf{A}^* \odot \mathbf{A})\mathbf{p}, \qquad (21)$$

where $\mathbf{A}^* \odot \mathbf{A} \in \mathbb{C}^{P^2 \times M}$ and $\odot$ denotes the Khatri-Rao product defined as a column-wise Kronecker product between two matrices with the same number of columns [26], [27].

For a Vandermonde matrix $\mathbf{A}$ defined as in (16), the matrix $\mathbf{A}^* \odot \mathbf{A}$ has full column rank if $M \leq 2P - 1$ [28]. Therefore, assuming this condition holds, (21) can be solved uniquely, i.e., we can recover the blood spectrum $\mathbf{p}$. Moreover, this condition allows to recover $\mathbf{p}$ while transmitting fewer Doppler pulses, as we show in the next subsection.

B. Nested Transmission Scheme

We now present a Doppler transmission scheme based on the concept of nested arrays [22], [29], [30], which has recently been considered in the fields of MIMO radar and DOA. A nested array is an array geometry obtained by systematically nesting two uniform linear arrays (ULA), which allows to resolve $O(N^2)$ signal sources using only N physical sensors when the second-order statistics of the received data is used. We adopt this concept and modify it for Doppler emissions with a fixed CPI (i.e., limited aperture).

Following the work in [22], we introduce two positive integers N_1, N_2 in the range $1 \leq N_1, N_2 \leq P$ such that

$$N_2(N_1 + 1) = P. \qquad (22)$$

We then choose the number of pulses to be $N = N_1 + N_2$. Notice that $N = N_1 + N_2 \leq P$ for any two positive integers satisfying (22). In the next section we will show how to choose N_1, N_2 in order to minimize N.

Given N_1 and N_2, we define the following two sets

$$\begin{aligned} \mathcal{S}_{\text{N}_1} &= \{1, 2, ..., N_1\}, \\ \mathcal{S}_{\text{N}_2} &= \{n(N_1 + 1), \quad n = 1, 2, ..., N_2\}. \end{aligned} \qquad (23)$$

Denote by $\mathcal{S}_{\text{N}}$ the ordered set of the union of $\mathcal{S}_{\text{N}_1}$ and $\mathcal{S}_{\text{N}_2}$

$$\mathcal{S}_{\text{N}} = \{\mathcal{S}_{\text{N}_1} \cup \mathcal{S}_{\text{N}_2}\}, \qquad (24)$$

which is referred to as a nested array. By varying N_1 and N_2 we generate different sets $\mathcal{S}_{\text{N}}$. Any set in this class is a concatenation of two ULAs with increasing inter-element spacing. Note that for $N_1 = P - 1$ and $N_2 = 1$ we have $\mathcal{S}_{\text{N}} = \{1, 2, ..., P\}$, hence, the standard transmission pattern is a special case of nested arrays.

Consider a non-uniform transmission pattern for spectral Doppler imaging such that the nth pulse is sent at time $p_n T$, where p_n is the nth element of $\mathcal{S}_{\text{N}}$, as illustrated in Fig. 1. In
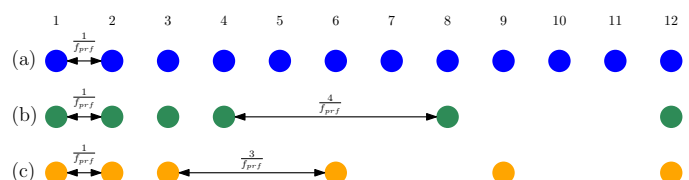

Fig. 1: **Transmission Patterns**. Different transmission patterns for an observation window of size $P = 12$, where every circle represents a Doppler pulse emission. (a) Standard transmission pattern. (b) Nested transmission pattern for $N_1 = N_2 = 3$. (c) Nested transmission pattern for $N_1 = 2$ and $N_2 = 4$.

this case, (4) becomes

$$s_{tx}(t) = \sum_{n=0}^{N-1} \sin\left(2\pi f_0 \big(t - (p_n - 1)T\big)\right), \qquad 0 \leq t \leq PT. \qquad (25)$$

Following the processing on the received signals described in Section II, the measured signal is written similarly to (16) as

$$y[k,n] = \sum_{m=1}^{M} \alpha_m \exp\left(2\pi j f_m (p_n - 1)T\right), \quad 0 \le n \le N-1. \tag{26}$$

In vector form we have

$$\mathbf{y}_N[k] = \mathbf{A}_N \boldsymbol{\alpha}, \tag{27}$$

where $\mathbf{y}_N[k] \in \mathbb{C}^{N \times 1}$ is the nested slow-time vector composed of samples from N emissions and $\mathbf{A}_N \in \mathbb{C}^{N \times M}$ is a matrix whose entries are given by $\mathbf{A}(n,m) = \exp\left(2\pi j f_m (p_n - 1)T\right)$. Note that $\mathbf{A}_N$ is constructed by choosing rows from the Vandermonde matrix $\mathbf{A}$, defined in (16), according to $\mathcal{S}_N$.

Denote the autocorrelation matrix $\mathbf{R}_{\mathbf{y}_N} = \mathbb{E}[\mathbf{y}_N \mathbf{y}_N^H] \in \mathbb{R}^{N \times N}$. Similarly to (19) and (21), we have

$$\mathbf{R}_{\mathbf{y}_N} = \mathbf{A}_N \mathbf{R}_{\boldsymbol{\alpha}} \mathbf{A}_N^H, \tag{28}$$

$$\mathbf{r}_N \triangleq \text{vec}(\mathbf{R}_{\mathbf{y}_N}) = (\mathbf{A}_N^* \odot \mathbf{A}_N)\mathbf{p} \triangleq \tilde{\mathbf{A}}\mathbf{p}. \tag{29}$$

In (29), the mth column of the matrix $\tilde{\mathbf{A}} \in \mathbb{C}^{N^2 \times M}$ has entries $\exp\left(2\pi j f_m (p_1 - p_2)\right)$ for $p_1, p_2 \in \mathcal{S}_N$, where p_1 and p_2 are pulse locations in the nested array $\mathcal{S}_N$. Defining the difference set of $\mathcal{S}_N$ as

$$\mathcal{D} = \{p_i - p_j \mid \quad p_i, p_j \in \mathcal{S}_N\}, \tag{30}$$

the entries of $\tilde{\mathbf{A}}$ are given by $\tilde{\mathbf{A}}(d,m) = \exp(2\pi j f_m p_d T)$ where p_d is the dth element of $\mathcal{D}$. Note that in our definition of $\mathcal{D}$, we allow repetition of its elements.

The system of equations defined in (29) can be solved uniquely if the matrix $\tilde{\mathbf{A}}$ has full column rank. Theorem 1 states necessary conditions for unique recovery. The theorem relies on the following lemma.

Lemma 1. *Let $\mathcal{D}_u$ be the set of unique elements of $\mathcal{D}$. Then, $\mathcal{D}_u$ consists of exactly $2N_2(N_1+1)-1$ distinct integers in the continuous range from $-N_2(N_1+1)+1$ to $N_2(N_1+1)-1$.*

Proof. See Appendix A. □

The number of degrees of freedom (DOF) of the nested set $\mathcal{S}_N$ is defined as the cardinality of the set $\mathcal{D}_u$. In our case, according to Lemma 1, the cardinality is equal to $|\mathcal{D}_u| = 2N_2(N_1+1)-1$. This number dictates the DOF of the system defined in (29) as stated in the next theorem, which follows directly from Lemma 1.

Theorem 1. *Let $\mathbf{A}_N \in \mathbb{C}^{N \times M}$ be the matrix defined in (28) with $|f_m| \le \frac{1}{2} f_{prf}$, $1 \le m \le M$. Then, the matrix $\tilde{\mathbf{A}} \triangleq (\mathbf{A}_N^* \odot \mathbf{A}_N) \in \mathbb{C}^{N^2 \times M}$ has exactly $2P-1$ distinct rows. It has full column rank if $2P > M$.*

Proof. Recall that the entries of $\tilde{\mathbf{A}}$ are given by $\tilde{\mathbf{A}}(d,m) = \exp(2\pi j f_m p_d)$. This implies that the dth row of $\tilde{\mathbf{A}}$ corresponds to the dth element of the difference set $\mathcal{D}$. Consequently, the number of distinct rows of $\tilde{\mathbf{A}}$ is equivalent to the number of unique elements of $\mathcal{D}$, which from Lemma 1 is $2N_2(N_1+1)-1$. Since $N_2(N_1+1) = P$, the matrix $\tilde{\mathbf{A}}$ has $2P-1$ distinct rows which correspond to a Vandermonde matrix. Hence, $\tilde{\mathbf{A}}$ is full column rank if $2P > M$. □

We can relate each element of the set $\mathcal{D}_u$ to a different time lag of the autocorrelation function of the slow-time signal. Thus, Lemma 1, followed by Theorem 1, ensures the recovery of all time lags of the autocorrelation function, i.e., the proposed transmission scheme satisfies the condition stated in [6]. This means that for $2P > M$, we can retrieve the power spectrum of the slow-time signal by exploiting its stationarity property and the lack of correlation between the amplitudes. As we prove below in Theorem 2, this may occur even for $N < P$.

C. Minimal Sampling Rate

We next derive the minimal number of Doppler transmissions which allow perfect spectrum recovery while using the nested emission scheme introduced in Subsection III-B.

Given an observation window of size P, we seek integers N_1 and N_2 which minimize the total number of Doppler transmissions N while maintaining the overall CPI. This can be cast as the following optimization problem:

$$\begin{aligned} &\min_{N_1, N_2 \in \mathbb{N}^+} \quad N_1 + N_2 \\ &\text{subject to} \quad N_2(N_1+1) = P. \end{aligned} \tag{31}$$

Note that whenever P is a prime number there is only one feasible solution $N_1 = P - 1$ and $N_2 = 1$, leading to the standard transmission scheme. Therefore, we treat the case in which P is not prime and (31) becomes a combinatorial optimization problem. A closed form solution to this problem is given by the following theorem.

Theorem 2. *Given an observation window of size P, let $\mathcal{D}_1$ and $\mathcal{D}_2$ be the sets defined as follows*

$$\mathcal{D}_1 = \{d|P : d \le \sqrt{P}\}, \quad \mathcal{D}_2 = \{d|P : d \ge \sqrt{P}\}.$$

Then, the optimum values for N_1 and N_2 are given by

$$\begin{aligned} N_1 &= \max(\mathcal{D}_1) - 1, \quad N_2 = \min(\mathcal{D}_2), \\ N_1 &= \min(\mathcal{D}_2) - 1, \quad N_2 = \max(\mathcal{D}_1). \end{aligned} \tag{32}$$

Proof. See Appendix B. □

Theorem 2 states that in the general case there are two optimal solutions (see Fig. 2). Note, however, that although both solutions offer the same minimal number of transmissions, they are not equivalent. A nested transmission scheme for given N_1 and N_2 creates $N_2 - 1$ gaps of size N_1 where no Doppler pulse is sent and can be used for B-mode. Therefore, the choice of N_1 and N_2 has an influence on the B-mode imaging, leading to a trade-off depending on the specific application. For example, in coherent plane-wave compounding [31], the size of the gap determines the number of inclination angles (i.e., image quality) while the number of gaps affects the image frame rate.

In the case where $\sqrt{P}$ is an integer we get that $\max(\mathcal{D}_1) = \min(\mathcal{D}_2) = \sqrt{P}$, leading to the following corollary:

Corollary 1. *Assuming $\sqrt{P} \in \mathbb{N}^+$, problem (31) has a unique solution. The minimal number of Doppler pulse emissions and the optimum values for N_1 and N_2 are given by*

$$N = 2\sqrt{P} - 1, \quad N_1 = \sqrt{P} - 1, N_2 = \sqrt{P}. \tag{33}$$

N_2	1	2	4	**8**	**16**	32	64	128
N_1	127	63	31	**15**	**7**	3	1	0
N	128	65	35	**23**	**23**	35	65	128

Fig. 2: **Nested Array Variations.** A summary of different variations of nested arrays for an observation window of size $P = 128$. The two optimal solutions are highlighted in red.

Theorem 2 along with Corollary 1 imply that when an observation window with size P is required, the blood power spectrum can be reconstructed from only $\Theta(\sqrt{P})$ Doppler pulse emissions. For example, given an observation window with $P = 256$, perfect spectrum recovery can be achieved from 31 Doppler transmissions, which is only 12% of the number of pulses sent in a standard transmission scheme. This reduction in the number of transmissions is greater than any previously proposed method.

IV. RECONSTRUCTION METHODS

We now consider two methods to reconstruct the blood power spectrum from sub-Nyquist slow-time samples obtained using the nested transmission scheme described in (29). We begin by introducing practical considerations into our framework.

First, we need to compute the autocorrelation matrix from which the subsequent signal model is derived. We estimate it by averaging samples over neighboring depths

$$\hat{\mathbf{R}}_{\mathbf{y}_{\mathrm{N}}} = \sum_{k=1}^{Q} \mathbf{y}_{\mathrm{N}}[k]\mathbf{y}_{\mathrm{N}}^{H}[k], \qquad (34)$$

where Q is proportional to f_s/f_0. Since the signal covariance matrix is estimated from a finite number of snapshots Q, the Khatri-Rao product in (29) is only an approximation. Moreover, we consider additive noise to the measurements, thus, we modify (27) to

$$\mathbf{y}_{\mathrm{N}}[k] = \mathbf{A}_{\mathrm{N}}\boldsymbol{\alpha} + \mathbf{w}[k], \qquad (35)$$

where $\mathbf{w}[k] \in \mathbb{C}^{N \times 1}$ is zero mean white complex Gaussian noise with unknown covariance matrix $\sigma^2 \mathbf{I}$, uncorrelated with the blood scatterers amplitudes. In this case, (28) and (29) become

$$\hat{\mathbf{R}}_{\mathbf{y}_{\mathrm{N}}} \approx \mathbf{A}_{\mathrm{N}}\mathbf{R}_{\boldsymbol{\alpha}}\mathbf{A}_{\mathrm{N}}^{H} + \sigma^2 \mathbf{I}_{N \times N}, \qquad (36)$$

$$\mathbf{r}_{\mathrm{N}} = \mathrm{vec}(\hat{\mathbf{R}}_{\mathbf{y}_{\mathrm{N}}}) \approx \tilde{\mathbf{A}}\mathbf{p} + \sigma^2 \mathrm{vec}(\mathbf{I}_{N \times N}). \qquad (37)$$

Next, due to the repetition of elements in $\mathcal{D}$, we have redundancy in the system of equations defined in (37), namely, some of the rows of $\mathbf{A}$ are identical. To reduce the system of equations and the effect of noise, we define for every $d \in \mathcal{D}_u$ the set $\mathcal{M}_d$ that collects all the indices where d occurs in $\mathcal{D}$

$$\mathcal{M}_d = \{i \,|\, \mathcal{D}(i) = d\}. \qquad (38)$$

Then, we define a new vector $\mathbf{z} \in \mathbb{C}^{(2P-1) \times 1}$ given by

$$\mathbf{z}(i_d) = \frac{1}{|\mathcal{M}_d|} \sum_{i \in \mathcal{M}_d} \mathbf{r}_{\mathrm{N}}(i), \quad d \in \mathcal{D}_u, \qquad (39)$$

where i_d denotes the index of d in $\mathcal{D}_u$ and $|\mathcal{M}_d|$ is the cardinality of $\mathcal{M}_d$, namely, the number of times d occurs in $\mathcal{D}$. Writing (39) in vector form, we have

$$\mathbf{z} = \bar{\mathbf{A}}\mathbf{p} + \sigma^2 \bar{\mathbf{e}}, \qquad (40)$$

where $\bar{\mathbf{e}} \in \mathbb{R}^{(2P-1) \times 1}$ is all zeros except a 1 at the Pth position. The matrix $\bar{\mathbf{A}} \in \mathbb{C}^{(2P-1) \times M}$ has entries $\bar{\mathbf{A}}(d, m) = \exp(2\pi j f_m p_d T)$ where p_d is the dth element of $\mathcal{D}_u$. To solve (40), we present two techniques which recover the blood spectrum $\mathbf{p}$.

A. Discrete Recovery

Suppose, as in standard Doppler methods, we limit ourselves to the Nyquist grid so that $f_m T = i_m/\tilde{P}$ for every $1 \le m \le M$, where i_m is an integer in the range $0 \le i_m \le \tilde{P} - 1$ and $\tilde{P} = 2P - 1$. Note that our grid is twice as dense as standard Doppler techniques so that our resolution is increased by a factor of 2. In this case, $\bar{\mathbf{A}} = \mathbf{F}^H \in \mathbb{C}^{\tilde{P} \times \tilde{P}}$ where $\mathbf{F}$ is the FFT matrix and we have

$$\mathbf{z} = \mathbf{F}^H \mathbf{p} + \sigma^2 \bar{\mathbf{e}}. \qquad (41)$$

By taking the Fourier transform of (41) scaled by $\tilde{P}$ and using the fact that $\mathbf{F}\mathbf{F}^H = \tilde{P}\mathbf{I}$, we obtain

$$\tilde{\mathbf{z}} = \frac{1}{\tilde{P}}\mathbf{F}\mathbf{z} = \mathbf{p} + \frac{\sigma^2}{\tilde{P}}\mathbf{1}, \qquad (42)$$

where $\mathbf{1} \in \mathbb{R}^{\tilde{P} \times 1}$ is a vector of all ones.

Finally, we adopt ideas from denoising schemes presented in [32], [33], [34] and employ a soft thresholding operator $\Gamma_\lambda(x) \triangleq \max(x - \lambda, 0)$ on the spectral estimates, which decreases the noise variance and the effect of spurious frequencies resulting from the finite sample averaging. Thus, our estimate of the blood spectrum is given by

$$\hat{\mathbf{p}} = \Gamma_\lambda(\tilde{\mathbf{z}}), \qquad (43)$$

where $\lambda \ge 0$ is determined empirically and can be tuned in real-time according to the clinician's desire. The proposed technique is outlined in Algorithm 1 and is referred to as Nested Slow-Time (NEST).

Note that NEST differs from the estimator proposed in [6] since NEST is based on the nested transmission scheme. As we show later in Sections V and VI, there are different emission schemes that satisfy the condition stated in [6] which lead to different recovery results. Thus, the right choice of the subsampling strategy may be crucial for successful recovery. Furthermore, NEST consists of an additional denoising step given by soft-thresholding, which leads to a better estimate of the autocorrelation function.

Given N, the complexity of NEST is $O(N^2 Q + P \log P)$. For the minimal slow-time sampling rate $N^2 \propto P$ the complexity is $O(PQ + P \log P)$, making NEST suitable for real-time implementation on commercial systems.

The properties of the difference set $\mathcal{D}_u$ are emphasized in NEST. In particular, the fact that $|\mathcal{D}_u| = 2P - 1$ allows to achieve spectral estimates with increased resolution of $2\pi/(2P - 1)T$, almost twice the resolution of standard processing. Moreover, since the elements of $\mathcal{D}_u$ are a filled ULA, the matrix $\bar{\mathbf{A}}$ reduces to a full FFT matrix, leading to an efficient implementation.

Algorithm 1 NEsted Slow-Time (NEST)

Input: Nested samples $\{\mathbf{y}[k]\}_{k=1}^{Q}$, threshold $\lambda \geq 0$.
　1: Estimate $\hat{\mathbf{R}}_{\mathbf{y}_N}$ by (34).
　2: Form $\mathbf{r}_N = \text{vec}(\hat{\mathbf{R}}_{\mathbf{y}_N})$.
　3: Compute $\mathbf{z}$ using (39).
　4: Apply a Fourier transform: $\tilde{\mathbf{z}} = \frac{1}{P}\mathbf{Fz}$ with $\tilde{P} = 2P - 1$.
　5: Apply soft-thresholding: $\mathbf{p} = \Gamma_\lambda(\tilde{\mathbf{z}})$.
Output: $\mathbf{p}$ - Blood power spectrum.

B. Continuous Recovery

In reality, grid-based methods exhibit estimation errors since the true Doppler frequencies are unlikely to lie on a predefined grid, regardless of how finely it is defined [35], [36]. To address this issue, we next provide a continuous recovery method which does not assume an underlying grid. This technique is based on the work in [36], [37] and depends on the eigenspace of the covariance matrix. Following [38], we construct a matrix $\widetilde{\mathbf{R}}$ given by the following theorem, which shares the same eigenspace as the covariance matrix.

Theorem 3. *Let* $\widetilde{\mathbf{R}}$ *be the following Toeplitz matrix*

$$\widetilde{\mathbf{R}} \triangleq \begin{pmatrix} \mathbf{z}(P) & \mathbf{z}(P-1) & \dots & \mathbf{z}(1) \\ \mathbf{z}(P+1) & \mathbf{z}(P) & \dots & \mathbf{z}(2) \\ \vdots & \vdots & \ddots & \vdots \\ \mathbf{z}(2P-1) & \mathbf{z}(2P-2) & \dots & \mathbf{z}(P) \end{pmatrix}. \quad (44)$$

For an infinite number of snapshots, the matrix $\widetilde{\mathbf{R}}$ *can be expressed as*

$$\widetilde{\mathbf{R}} = \mathbf{A}\mathbf{R}_\alpha\mathbf{A}^H + \sigma^2\mathbf{I}_{P\times P},$$

where $\mathbf{A}$ *and* $\mathbf{R}_\alpha$ *are defined in (16) and (19) respectively.*

Proof. See [38]. □

Note that in practice we have a finite number of snapshots, hence, the structure of $\widetilde{\mathbf{R}}$ given by Theorem 3 holds only approximately. Nevertheless, from Theorem 3 it follows that in the absence of noise, the range space of $\widetilde{\mathbf{R}}$ is identical to that of $\mathbf{A}$. This special structure can be exploited to recover the Doppler frequencies by using subspace methods [39]. We now briefly describe the ESPRIT algorithm [40], [39], provided as a representative of subspace approaches.

Assuming M is known, let $\mathbf{E}_M$ denote the matrix of size $P \times M$ consisting of the eigenvectors corresponding to the M largest eigenvalues of $\widetilde{\mathbf{R}}$. Since the matrices $\mathbf{A}$ and $\mathbf{E}_M$ span the same space, there exists an invertible $M \times M$ matrix $\mathbf{T}$ such that

$$\mathbf{A} = \mathbf{E}_M\mathbf{T}. \quad (45)$$

Let $\mathbf{V}_1$ be the $P-1 \times M$ matrix consisting of the first $P-1$ rows of $\mathbf{A}$, and let $\mathbf{V}_2$ be the $P-1 \times M$ matrix consisting of the last $P-1$ rows of $\mathbf{A}$. Then, we have that

$$\mathbf{V}_2 = \mathbf{V}_1\Lambda, \quad (46)$$

where $\Lambda \in \mathbb{C}^{M\times M}$ is a diagonal matrix with entries $\Lambda(m,m) = \exp(2\pi j f_m T)$. In addition, let $\mathbf{E}_1$ and $\mathbf{E}_2$ be equal to the first and last $P-1$ rows of $\mathbf{E}_M$ respectively. From (45), we get

$$\begin{aligned} \mathbf{V}_1 &= \mathbf{E}_1\mathbf{T}, \\ \mathbf{V}_2 &= \mathbf{E}_2\mathbf{T}. \end{aligned} \quad (47)$$

Combining (46) and (47) leads to the following relation between the matrices $\mathbf{E}_1$ and $\mathbf{E}_2$:

$$\mathbf{E}_2 = \mathbf{E}_1\mathbf{T}\Lambda\mathbf{T}^{-1}. \quad (48)$$

Assuming $M \leq P - 1$, the matrix $\mathbf{E}_1$ is full column rank, therefore, $\mathbf{E}_1^\dagger\mathbf{E}_1 = \mathbf{I}$ where $\mathbf{E}_1^\dagger$ is the pseudo-inverse of $\mathbf{E}_1$. Multiplying (48) on the left by $\mathbf{E}_1^\dagger$ leads to

$$\mathbf{E}_1^\dagger\mathbf{E}_2 = \mathbf{T}\Lambda\mathbf{T}^{-1}. \quad (49)$$

Following (49), we can recover the Doppler frequencies from the eigenvalues of $\mathbf{E}_1^\dagger\mathbf{E}_2$.

ESPRIT requires knowledge of the number of Doppler frequencies M, which is typically unavailable to us. In practice, one can estimate M using, for example, the minimum description length (MDL) algorithm [40]. Here, we propose an alternative based on low rank approximation [37].

Let the eigen-decomposition of $\widetilde{\mathbf{R}}$ be given by

$$[\mathbf{E}, \mathbf{d}] = \text{eig}(\widetilde{\mathbf{R}}), \quad (50)$$

where $\mathbf{E}$ consists of the eigenvectors in its columns and $\mathbf{d}$ is a vector consisting of the eigenvalues in a non-increasing order. To promote low rank of the matrix $\widetilde{\mathbf{R}}$, we perform soft-thresholding on $\mathbf{d}$ and estimate M as

$$M = ||\Gamma_\lambda(\mathbf{d})||_0, \quad (51)$$

where $\lambda \geq 0$ is chosen empirically and $||\cdot||_0$ is the l_0 semi-norm which counts the number of nonzero elements of the vector. This operation acts as a denoising scheme and accounts for the finite snapshot effect on the estimates. Given the estimate of M, we define $\mathbf{E}_M$ as the first M columns of $\mathbf{E}$ and perform ESPRIT as described.

Once the Doppler frequencies are recovered, the Vandermonde matrix $\bar{\mathbf{A}}$, defined in (40), is constructed. Assuming $2P > M$ the matrix $\bar{\mathbf{A}}$ has full column rank and the blood spectrum vector $\mathbf{p}$ is then obtained by left inverting $\bar{\mathbf{A}}$,

$$\hat{\mathbf{p}} = \bar{\mathbf{A}}^\dagger\mathbf{z}. \quad (52)$$

The proposed recovery method is summarized in Algorithm 2 and is referred to as NESPRIT.

The NESPRIT algorithm can theoretically exhibit infinite frequency-precision in identifying the Doppler frequencies when there is no noise. However, it has a large computational load. The complexity of NESPRIT is dominated by the eigen-decomposition of a $P \times P$ Hermitian matrix, which requires $O(P^3)$ operations [41]. Note, however, that more computationally efficient methods, presented in [42], may be used to reduce the complexity of traditional ESPRIT.

Algorithm 2 NEsted Slow-Time ESPRIT (NESPRIT)

Input: Nested samples $\{\mathbf{y}[k]\}_{k=1}^{Q}$, threshold $\lambda \geq 0$.
  1 : Estimate $\hat{\mathbf{R}}_{\mathbf{y}_N}$ by (34).
  2 : Form $\mathbf{r}_N = \text{vec}(\hat{\mathbf{R}}_{\mathbf{y}_N})$.
  3 : Compute $\mathbf{z}$ using (39).
  4 : Construct $\widetilde{\mathbf{R}}$ according to (44).
  5 : Decompose $\widetilde{\mathbf{R}}$: $[\mathbf{E}, \mathbf{d}] = \text{eig}(\widetilde{\mathbf{R}})$.
  6 : Estimate $M = ||\Gamma_\lambda(d)||_0$.
  7 : Extract $\mathbf{E}_M = [\mathbf{e}_1, \ldots, \mathbf{e}_M]$.
  8 : Define $\mathbf{E}_1$ and $\mathbf{E}_2$ as in (47).
  9 : Compute the eigenvalues of $\mathbf{E}_1^\dagger \mathbf{E}_2$: $\boldsymbol{\beta} = \text{eig}(\mathbf{E}_1^\dagger \mathbf{E}_2)$.
  10: Estimate the Doppler frequencies $\boldsymbol{f} = \frac{\angle \boldsymbol{\beta}}{2\pi T}$
  11: Construct $\bar{\mathbf{A}}$ defined in (40) using $\boldsymbol{f}$.
  12: Spectrum recovery: $\mathbf{p} = \bar{\mathbf{A}}^\dagger \mathbf{z}$
Output: $(\boldsymbol{f}, \mathbf{p})$ - Blood power spectrum.

C. Clutter Filtering and Apodization

One major challenge in spectral Doppler is clutter filtering. Clutter signals stem from backscattered echoes from vessel's walls and surrounding tissues, stationary and non-stationary, and are typically 40 to 60 dB stronger than the flow signal [43], [1], [44]. Thus, clutter may obscure blood velocities and must be removed for accurate velocity estimation.

Conventionally, clutter removal is applied using high-pass finite impulse response (FIR) filters or infinite impulse response (IIR) filters. However, such filters assume uniformly sampled data, which is not the case when using sparse Doppler sequences. To overcome this, in [6], [10], polynomial regression filters were used for clutter rejection since they are not restricted to uniform sampling. The downside of regression filters is that they may lead to spurious frequencies in the output spectrum [45], [12], compromising their reliability for clinical use.

A crucial disadvantage of many sparse Doppler methods is their inability to use FIR and IIR filters for clutter removal. Fortunately, NEST and NESPRIT do not share this limitation, since they recover the full uniform autocorrelation function, allowing to perform filtering in the correlation domain as we show next.

Consider a linear time invariant (LTI) stable system with impulse response $h[n]$, driven by a WSS discrete process $x[n]$. Denoting by $y[n]$ the output of the system and by $R_y[n]$ the autocorrelation function of $y[n]$, we have

$$
\begin{aligned}
y[n] &= x[n] * h[n] \\
R_y[n] &= R_x[n] * h[n] * h[-n],
\end{aligned} \tag{53}
$$

where $R_x[n]$ is the autocorrelation function of the input and $*$ denotes convolution. Following (53), any FIR or IIR filter $h[n]$ can be applied in the correlation domain by computing

$$
\tilde{\mathbf{z}}[n] = \mathbf{z}[n] * h[n] * h[-n], \tag{54}
$$

where $\mathbf{z}[n]$ is given by (39). Thus, the fact that we recover the full uniform autocorrelation function allows us to perform clutter removal using any desired filter. In addition, specifically for NESPRIT, which involves an eigenvalue decomposition, eigen-based clutter filters [46] are directly applicable.

Similarly, any apodization function $a[n]$, used for reducing sidelobes, may be applied directly in the correlation domain by computing

$$
\hat{\mathbf{z}}[n] = \mathbf{z}[n] \cdot R_a[n], \tag{55}
$$

where $\mathbf{z}[n]$ is given by (39) and $R_a[n]$ is the autocorrelation function of $a[n]$.

V. Alternative Sparse Arrays

So far, we considered only nested arrays as an approach for reducing the number of Doppler transmissions. However, in the literature of array processing there are alternative sparse array configurations which can match the performance of their fully populated counterparts. In this section, we briefly review several alternatives and discuss their properties in comparison with nested arrays.

A. Super Nested

A modified version of nested arrays are the super nested arrays [47], [48], [49]. Assuming $N_1 \geq 4$ and $N_2 \geq 3$, super nested arrays are specified by the integer set $\mathcal{S}_{SN}$ created by concatenating six ULAs (see Fig. 3), defined by

$$
\begin{aligned}
\mathcal{S}_{SN} &= \mathcal{X}_1 \cup \mathcal{Y}_1 \cup \mathcal{X}_2 \cup \mathcal{Y}_2 \cup \mathcal{Z}_1 \cup \mathcal{Z}_2, \\
\mathcal{X}_1 &= \{1 + 2l \,|\, 0 \leq l \leq A_1\}, \\
\mathcal{Y}_1 &= \{(N_1 + 1) - (1 + 2l) \,|\, 0 \leq l \leq B_1\}, \\
\mathcal{X}_2 &= \{(N_1 + 1) + (2 + 2l) \,|\, 0 \leq l \leq A_2\}, \\
\mathcal{Y}_2 &= \{2(N_1 + 1) - (2 + 2l) \,|\, 0 \leq l \leq B_2\}, \\
\mathcal{Z}_1 &= \{l(N_1 + 1) \,|\, 2 \leq l \leq N_2\}, \\
\mathcal{Z}_2 &= \{N_2(N_1 + 1) - 1\}
\end{aligned} \tag{56}
$$

with

$$
(A_1, B_1, A_2, B_2) = \begin{cases}
(r, r-1, r-1, r-2), & N_1 = 4r, \\
(r, r-1, r-1, r-1), & N_1 = 4r+1, \\
(r+1, r-1, r-1, r-2), & N_1 = 4r+2, \\
(r, r, r, r-1), & N_1 = 4r+3,
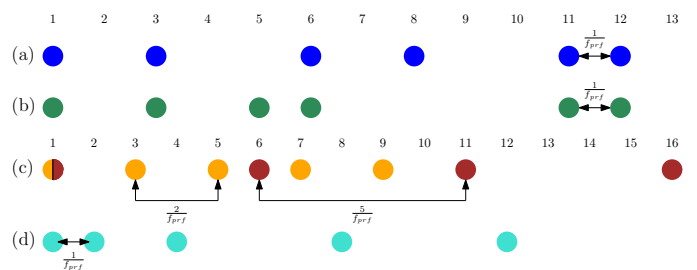\end{cases}
$$

where r is an integer.

Fig. 3: **Alternative Transmission Patterns.** Different transmission patterns for various observation windows. (a) Super nested pattern for $N_1 = N_2 = 3$, $P = 12$. (b) 3rd order super nested pattern for $N_1 = N_2 = 3$, $P = 12$. (c) Co-prime scheme for $N_1 = 2, N_2 = 5$, $P = 11$, where a two color circle represents a single Doppler transmission that is mutual for both sub-arrays. (d) 3-level nested array for $N_1 = N_2 = 1$, $N_3 = 3$, $P = 12$. Matlab code for generating super nested arrays can be found in [50].

These variants share the same properties as nested arrays in terms of the number of Doppler transmissions and their

difference sets. In addition, they offer an advantage over nested arrays of reduced mutual coupling [51], which in our case translates to the effect of previous transmissions on the received signal corresponding to the current emission. This property may allow increasing the maximal depth examined. However, super nested arrays exhibit complex geometry compared to nested arrays. In particular, the Doppler gaps created are not of the same size and thus using them for B-mode imaging may be difficult in certain applications.

B. Co-Prime Array

This type of sparse array has been studied extensively in the literature [52], [53], [54], [55], [56], [57], [58]. Let $N_1 < N_2$ be co-prime integers, i.e., their greatest common divisor (gcd) is 1. A co-prime array is composed of two ULAs with inter-element spacing N_1 and N_2:

$$
\begin{aligned}
\mathcal{S}_{N_1} &= \{n_1 N_2, \quad n_1 = 0, 1, ..., 2N_1 - 1\}, \\
\mathcal{S}_{N_2} &= \{n_2 N_1, \quad n_2 = 0, 1, ..., N_2 - 1\}, \\
\mathcal{S}_{CP} &= \{\mathcal{S}_{N_1} \cup \mathcal{S}_{N_2}\}.
\end{aligned}
\tag{57}
$$

By Lemma 1 in [54], the difference set of $\mathcal{S}_{CP}$ contains all $2N_1 N_2 + 1$ contiguous integers from $-N_1 N_2$ to $N_1 N_2$. This means that for an appropriate choice of N_1 and N_2 such that $N_1 N_2 = P - 1$, we can recover all time lags of the autocorrelation from $-(P-1)$ to $P-1$ with a roughly equal number of correlation pairs for all lags. In addition, a co-prime array has the property of reduced mutual coupling compared to a nested array, while having a simpler geometry compared to super nested arrays.

The main drawback of co-prime arrays is that they require sending Doppler pulses in times beyond the observation window, as can be seen in Fig. 3. Therefore, the reflected slow-time signal may not preserve its stationarity property, which is a key assumption in Doppler processing. To overcome this, we can limit ourselves to Doppler transmissions sent within the observation window. However, in this case, the difference set is not a filled ULA, i.e., not all time lags are recovered. As a result, this will reduce the number of DOF, namely, the number of velocities that are recoverable.

C. K-Level Nested Array

The nested array concept is based on concatenating two ULAs. A *K-Level nested array* is an extension to K ULAs. This array is parameterized by $K, N_1, N_2, ..., N_K \in \mathbb{N}^+$ and defined as follows:

$$
\begin{aligned}
\mathcal{S}_1 &= 1, 2, ..., N_1, \\
\mathcal{S}_i &= \left\{ n \prod_{j=1}^{i-1} (N_j + 1), \quad n = 1, 2, ..., N_i \right\} \quad i = 2, 3, ..., K, \\
\mathcal{S}_{KL} &= \bigcup_{i=1}^{K} \mathcal{S}_i.
\end{aligned}
\tag{58}
$$

The inter-element spacing in the ith level is equal to $N_{i-1} + 1$ times the spacing in the $(i-1)$th level, as illustrated in Fig. 3.

To determine the minimal number of transmissions using this approach, we define a generalized version of problem (31):

$$
\min_{K \in \mathbb{N}^+} \quad \min_{N_1, ..., N_K \in \mathbb{N}^+} \quad \sum_{i=1}^{K} N_i
$$
$$
\text{subject to} \qquad N_k \prod_{i=1}^{K-1} (N_i + 1) = P.
\tag{59}
$$

The solution to (59) is given by the following theorem.

Theorem 4. *Let P be the size of a given observation window, represented by its prime factorization*

$$
P = \prod_{i=1}^{\omega} p_i^{q_i},
$$

where ω is the number of distinct prime factors of P. Define $\Omega = \sum_{i=1}^{\omega} q_i$. The optimal number of nesting levels K and the minimal number of transmissions are given by

$$
K = \Omega,
$$
$$
N = 1 + \sum_{i=1}^{\omega} (p_i - 1) q_i,
$$
$$
\{N_i\}_{i=1}^{\Omega} = \Big\{ \underbrace{p_1 - 1, ..., p_1 - 1}_{q_1 \, times}, ..., \underbrace{p_\omega - 1, ..., p_\omega - 1}_{q_\omega - 1 \, times}, p_\omega \Big\}.
$$

Proof. See Appendix C. □

A common choice for P is a power of two. The optimal K-level nested array in this case is given by the following corollary:

Corollary 2. *Consider an observation window of size $P = 2^n$ for some $n \in \mathbb{N}^+$. The optimal transmission pattern consists of $n + 1$ emissions with exponential spacing, given by the set*

$$
\mathcal{S}_{opt} = \{1, 2, 4, ...2^n\}.
$$

Nested arrays are associated with second-order statistics while K-level nested arrays extend this notion to higher-order statistics. For example, 4-level nested arrays are related to differences of the difference set, i.e. 4th-order moments. Thus, if we consider higher-order statistics, then Theorem 4 implies that K-level nested arrays offer a significant reduction in the number of Doppler transmissions over nested arrays. However, using higher-order statistics requires a large number of snapshots, which may not be available.

VI. SIMULATIONS AND IN VIVO RESULTS

We now demonstrate blood spectrum reconstruction from sparse slow-time samples. The NEST and NESPRIT algorithms are evaluated using Field II [24], [25] simulations with the Womersley model [59] for pulsating flow from the femoral artery. The specific parameters for the Field II simulation of the flow are summarized in Table I. The estimation of the autocorrelation matrix was performed using $Q = 33$ regularly spaced samples along depth and involved subtraction of the mean of the signal, thus removing the signal's stationary part. In addition, the thresholding parameter in NEST was chosen

Transducer center frequency	f_0	3.5 [MHz]
Pulse repetition frequency	f_{prf}	5 [kHz]
Sampling frequency	f_s	20 [MHz]
Speed of sound	c	1540 [m/s]
Mean velocity		0.1 [m/s]
Beam/flow angle		60°
Observation window size	P	256

TABLE I: Parameters for femoral flow simulation

as $\lambda = \alpha \max(\tilde{\mathbf{z}})$ where $\alpha \in [0.2, 0.4]$ and $\mathbf{z}$ is given by (42). In NESPRIT, we set it to $\lambda = \beta \max(\mathbf{d})$ where $\beta \in [0.3, 0.7]$ and $\mathbf{d}$ is given by (50).

A. MSE versus SNR

First, we evaluate the performance of the proposed algorithms by using a simplified signal simulated according to (13), comprising a single Doppler frequency which does not lie on the grid of standard processing. We consider an observation window of size $P = 8$ and a nested transmission scheme where $N_1 = 3, N_2 = 2$ and $T = 1$. Assuming a Doppler frequency $f = 3/15 = 0.2$, we compare NEST, NESPRIT and Welch's method by studying the mean squared error (MSE) of their frequency estimates as a function of signal-to-noise ratio (SNR). We define the MSE of an estimate $\hat{f}$ as

$$MSE(\hat{f}) = \mathbb{E}[(f - \hat{f})^2], \qquad (60)$$

where $\mathbb{E}[\cdot]$ is the expectation operator evaluated empirically using 1000 Monte Carlo simulations.

Figure 4 shows the MSE of the three methods as a function of SNR for $Q = 200$ snapshots. Notice how the performance of the three methods improves considerably with increasing SNR. In low SNR regimes NEST performs the worst while the performance of NESPRIT and Welch's method are comparable. However, while from a certain point both NEST and NESPRIT recover the Doppler frequency perfectly, Welch's method still produces an error even in the high SNR regime. This is expected due to the limited Doppler resolution of Welch's method compared to NEST and NESPRIT.
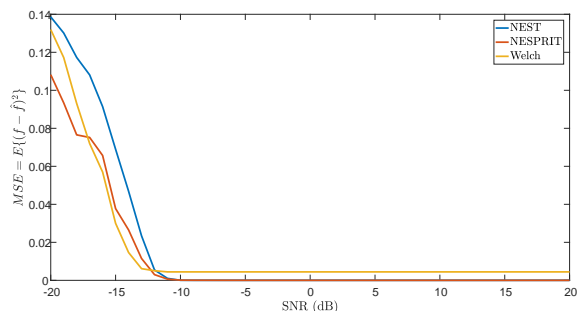

Fig. 4: **MSE versus SNR.** MSE as a function of SNR (for a single Doppler frequency) of NEST and NESPRIT methods applied for a nested transmission scheme with $N_1 = 3$, $N_2 = 2$ and $Q = 33$.

B. Different Slow-Time Subsampling Levels

We now investigate the spectrum recovery of NEST and NESPRIT using the proposed sparse transmission scheme with different levels of slow-time subsampling, i.e., different number of Doppler emissions:

1) $N = 129 \, (\approx 50.3\%) : N_1 = 127, N_2 = 2$
2) $N = 67 \, (\approx 26.1\%) \ : N_1 = 63, N_2 = 4$
3) $N = 39 \, (\approx 15.2\%) \ : N_1 = 31, N_2 = 8$.

Figure 5 shows the spectrogram of traditional Welch's method and the ones obtained with NEST (top) and NESPRIT (bottom) using 50.3%, 26.1% and 15.2% of possible Doppler transmissions. As can be seen, for all levels of subsampling both proposed algorithms produce a clear and accurate spectrogram. This allows the user the freedom to vary N_1 and N_2 and thus determine the level of subsampling dynamically.

C. Clutter Filter and Apodization

Next we demonstrate the application of clutter filtering and apodization using NEST and NESPRIT techniques. To that end, a clutter signal was superimposed on the flow model being 40 dB stronger than the blood signal. We use a Butterworth high pass filter with normalized cutoff frequency 0.03 and apodization with a Hamming window of length 256. Recall that these actions are performed on the autocorrelation signal given by (39).

Figure 6 presents spectrograms of NEST (top) and NESPRIT (bottom) reconstructed from approximately 25% of the Doppler emissions. On the left side the resultant unfiltered spectrograms are given. As seen, only the frequency related to the clutter signal is visible, since the clutter obscures the blood velocities entirely. Applying a high pass filter on the autocorrelation signal produces adequate spectrograms (middle) where clearly the low frequencies are filtered out. As expected, there are artifacts due to the fact that the filtering is not ideal and part of the blood signal is also filtered out along with the clutter. Using Hamming apodization helps in reducing these artifacts, yielding cleaner spectrograms (right).

These last results emphasize the importance of recovering the slow-time autocorrelation which allows to incorporate any conventional clutter filter and apodization in NEST and NESPRIT.

D. Alternative Sampling Patterns

Here we examine other transmission schemes reviewed in Section V. In Fig. 7 the spectrograms recovered by NEST (top) and NESPRIT (bottom) are presented, where the input vector was acquired in each setting according to a different transmit pattern - super-nested (left), co-prime (middle), 4-level nested (right). The parameters of each emission scheme are presented in Table II. As can be seen in Fig. 7, for co-prime and 4-level nested patterns, NEST and NESPRIT failed to produce clear spectrograms and exhibit severe artifacts. This is expected since when using these transmit schemes the resulting autocorrelations have holes, leading to aliasing which is dramatic especially when the spectrum consists of a wide range of frequencies. Note that for the 4-level nested scheme, NESPRIT failed to produce a visible spectrogram and hence is not shown. Moreover, the spectrograms resulting from the super-nested pattern, although clear, exhibit aliasing which is
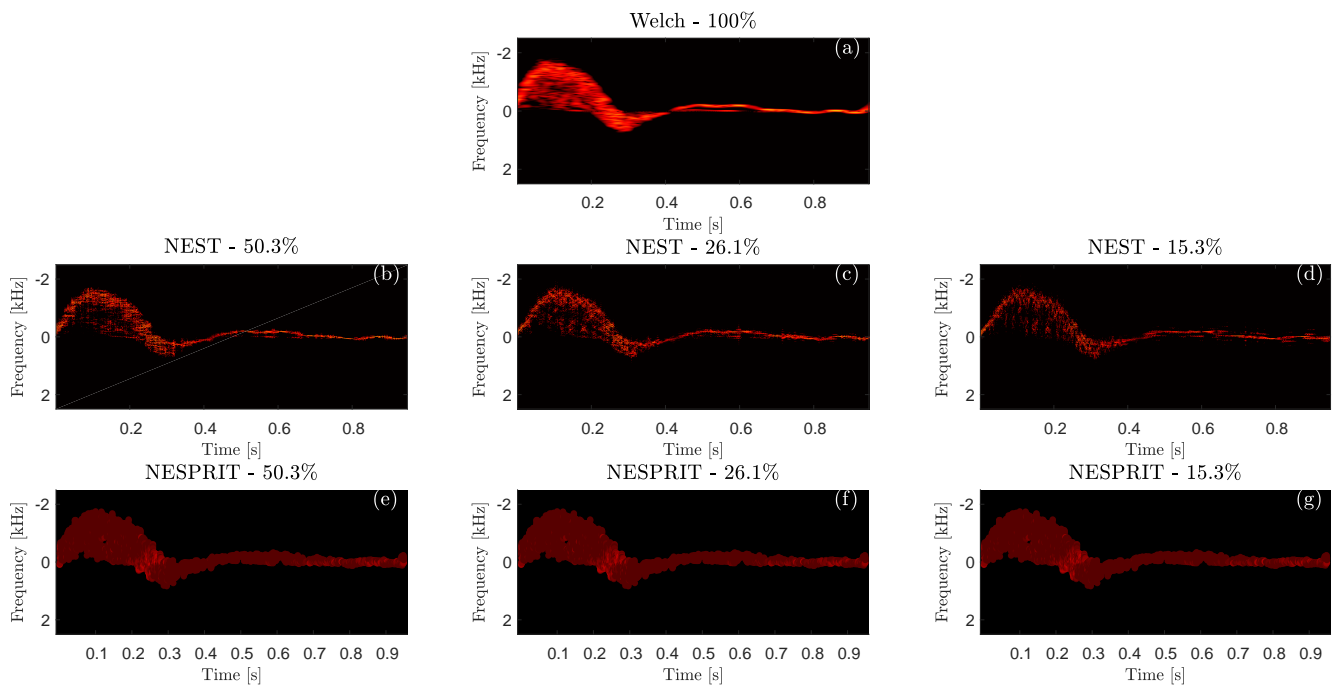
Fig. 5: **Different Subsampling Levels.** Spectrograms of the simulated femoral artery using different slow-time subsampling from 256 pulses (100%) down to 39 pulses (≈15%). (a) Welch's method - 100% (b) NEST - 50.3% (c) NEST - 26.1% (d) NEST - 15.2% (e) NESPRIT - 50.3% (f) NESPRIT - 26.1% (g) NESPRIT - 15.2%. All spectrograms are displayed with a dynamic range of 60 dB.
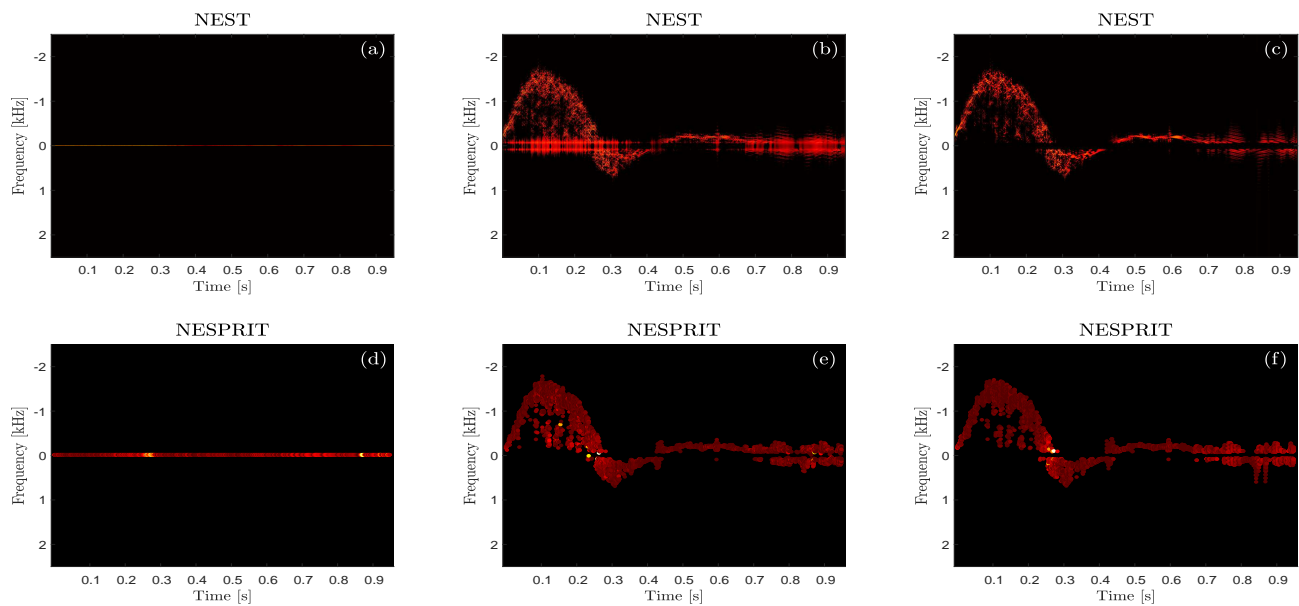

Fig. 6: **Clutter Filtering and Apodization.** Spectrograms of the simulated femoral artery with superimposed clutter signal. (a) NEST with no filter (b) NEST with high pass filter (c) NEST with high pass filter and Hamming apodization (d) NESPRIT with no filter (e) NESPRIT with high pass filter (f) NESPRIT with high pass filter and Hamming apodization. All spectrograms reconstructed using only 67 transmissions (25%) and displayed with a dynamic range of 60 dB.

Super-nested	$N_1 = 15$ $N_2 = 16$
Co-prime	$N_1 = 14$ $N_2 = 9$
4-Level nested	$N_1 = N_2 = N_3 = 3$ $N_4 = 4$

TABLE II: Parameters for different transmit patterns

surprising because the super-nested approach shares the nested pattern property of having a full autocorrelation. This aliasing is probably due to the fact that in super-nested transmission there is only one pair of transmissions separated in time by T, which may lead to inaccurate estimation of lag one of the autocorrelation, effectively reducing the PRF by a factor of 2.

E. Minimal Rate Performance

As a final simulation, we test the performance of both NEST and NESPRIT for the minimal slow-time sampling rate. According to the nested approach, for an observation window of size $P = 256$ the minimal number of Doppler transmissions is $2\sqrt{P} - 1 = 31$, which is 12% of 256. Based on this subsampling scheme, the proposed techniques are compared with the conventional Welch's method and with two recent developed techniques BSLIM and BIAA which can handle arbitrary sampling schemes of the slow-time data. The resulting spectrograms are shown in Fig. 8. As can be seen, the blood spectrograms formed by NEST and NESPRIT are sharp and clear, whereas, Welch's method, BSLIM and BIAA produce spectrograms with significant artifacts, especially in regions of high velocities due to aliasing. These last results prove that NEST and NESPRIT, based on the proposed transmission scheme, are able to fully recover the blood spectrum only from 12%. This along with the fact that NEST and NESPRIT present a closed form solution, in contrast to other competitive methods, indicate that NEST and NESPRIT outperform current state-of-the-art techniques.

F. In vivo

We end by evaluating the performance of the proposed methods on in vivo data obtained online[1]. The data consists of a Carotid artery of a healthy volunteer examined using a B-K 8556 ultrasound scanner with a 3.2 MHz linear array probe transducer in duplex mode. The sampling frequency was 8 kHz and the pulse repetition frequency was 3.5 kHz. An observation window of $P = 128$ samples was chosen. The data was synthetically undersampled according to the nested transmission scheme with $N_1 = 31$ and $N_2 = 4$ for both NEST and NESPRIT, leading to a total number of 35 emissions ($\sim 27\%$). The obtained spectrograms are shown in Fig. 9. As can be seen from the figure, NEST and NESPRIT successfully recover the Doppler frequencies from a small number of transmissions, producing similar spectrograms to that obtained by Welch's method using the fully sampled data. These results validate the effectiveness of the proposed methods and their potential for clinical use.

[1]The data was downloaded from http://bme.elektro.dtu.dk/31545/.

VII. Conclusion

In this paper, we presented a sparse irregular transmission scheme for medical spectral Doppler based on nested arrays. Using this approach, we showed that in noiseless settings the blood spectrum can be recovered from only $2\sqrt{P} - 1$ emissions, where P is the size of the observation window. Two recovery algorithms NEST and NESPRIT, which exploit the proposed transmission pattern, were presented. NEST exhibits low complexity and performs efficient reconstruction of the blood spectrum with enhanced resolution. NESPRIT theoretically achieves infinite frequency-precision in recovering the blood velocities at the expense of computational load. Moreover, any clutter filter and apodization function can be easily incorporated into NEST and NESPRIT. Both algorithms were evaluated and tested with Field II simulation data of pulsating flow from the femoral artery. NEST and NESPRIT were compared and shown to outperform current state-of-the-art methods by successfully recovering the blood spectrum from only 12% of the Doppler transmissions. Finally, in vivo results showed the ability of the proposed techniques to yield valid spectrograms using far fewer emissions, proving their potential for clinical use. This paves the way for duplex mode imaging, displaying high resolution blood spectrograms while providing high quality B-mode images at a high frame rate.

Appendix A
Proof of Lemma 1

First, it easy to see that the maximal difference in absolute values between elements of $\mathcal{S}_N$ is $N_2(N_1 + 1) - 1$. Hence, there is no integer k such that $|k| > N_2(N_1 + 1) - 1$ which belongs to $\mathcal{D}$ or $\mathcal{D}_u$.

Given any integer k in the range $-N_2(N_1 + 1) + 1 \leq k \leq N_2(N_1 + 1) - 1$, we have that $k \in \mathcal{D}_u$ if there exists p_i and p_j which satisfy

$$k = p_i - p_j, \quad p_i, p_j \in \mathcal{S}_N. \tag{61}$$

Note that if for a specific k there exists such $p_i, p_j \in \mathcal{S}_N$, i.e., $k \in \mathcal{D}_u$, then also $-k \in \mathcal{D}_u$ since

$$-k = -(p_i - p_j) = p_j - p_i. \tag{62}$$

Therefore, we focus on proving (61) only for non-negative integers k in the range $0 \leq k \leq N_2(N_1 + 1) - 1$.

Every integer k in the desired range can be decomposed as

$$k = m(N_1 + 1) + r, \tag{63}$$

where m and r are integers in the ranges $0 \leq m \leq N_2 - 1$ and $0 \leq r \leq N_1$, respectively. Denoting $p_i = (m+1)(N_1+1)$ and $p_j = N_1 + 1 - r$, we can rewrite (63) as

$$\begin{aligned} k = m(N_1 + 1) + r = \\ = (m + 1)(N_1 + 1) + r - N_1 - 1 = \\ = (m + 1)(N_1 + 1) - (N_1 + 1 - r) = \\ = p_i - p_j. \end{aligned} \tag{64}$$

By definition $p_i \in \mathcal{S}_{N_2}$. When $r = 0$, $p_j \in \mathcal{S}_{N_2}$; otherwise $p_j \in \mathcal{S}_{N_1}$. Thus, $p_i, p_j \in \mathcal{S}_N$ and we conclude that $k \in \mathcal{D}_u$.
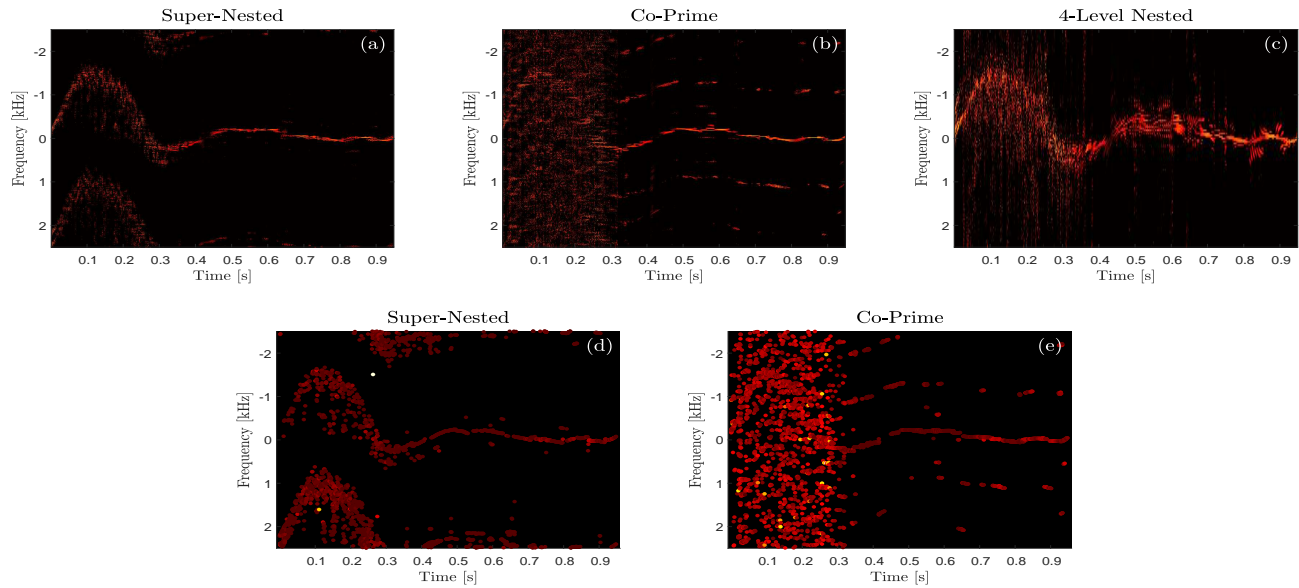
Fig. 7: **Alternative Transmission Schemes.** Spectrograms of the simulated femoral artery using alternative emission patterns. (a) Super-Nested scheme with NEST recovery (b) Co-Prime scheme with NEST recovery (c) 4-Level Nested with NEST recovery (d) Super-Nested scheme with NESPRIT (e) Co-Prime scheme with NESPRIT recovery. All spectrograms are displayed with a dynamic range of 60 dB.
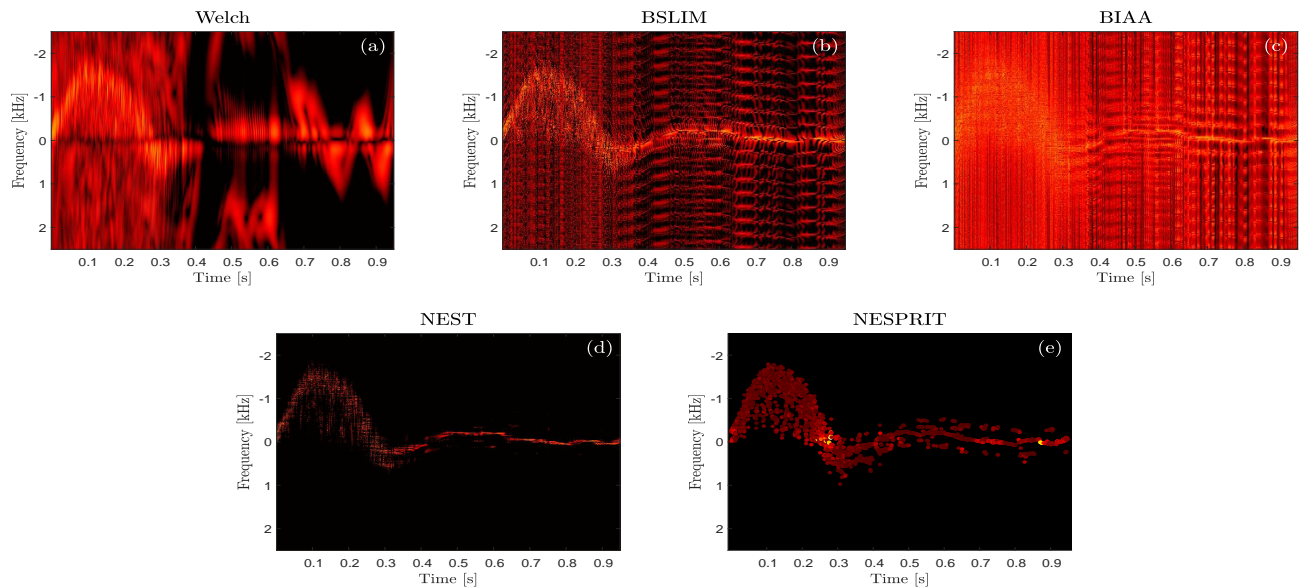

Fig. 8: **Performance Comparison for Minimal Rate.** Spectrograms of the simulated femoral artery using only 31 pulses out of 256 (12%) according to the sparse emission scheme. (a) Welch's method (b) BSLIM (c) BIAA (d) NEST (e) NESPRIT. All spectrograms are displayed with a dynamic range of 60 dB.

APPENDIX B
PROOF OF THEOREM 2

Denoting $\tilde{N}_1 = N_1 + 1$, we recast problem (31) as follows

$$\begin{aligned} \min_{\substack{\tilde{N}_1, N_2 \in \mathbb{N}^+ \\ \tilde{N}_1 \geq 2}} \quad & \tilde{N}_1 + N_2 - 1 \\ \text{subject to} \quad & N_2 \tilde{N}_1 = P. \end{aligned} \tag{65}$$

From (65), it is easy to see that $N_2 = \frac{P}{\tilde{N}_1}$, where $\tilde{N}_1$ is a divisor of P. Assuming $\tilde{N}_1 \leq N_2$, we have

$$\tilde{N}_1 = \operatorname*{argmin}_{\mathcal{D}_1} \quad d + \frac{P}{d}, \tag{66}$$

where we neglect the constant term -1.

Next, we define a function $f : [1, \sqrt{P}] \to \mathcal{R}^+$ over a continuous domain
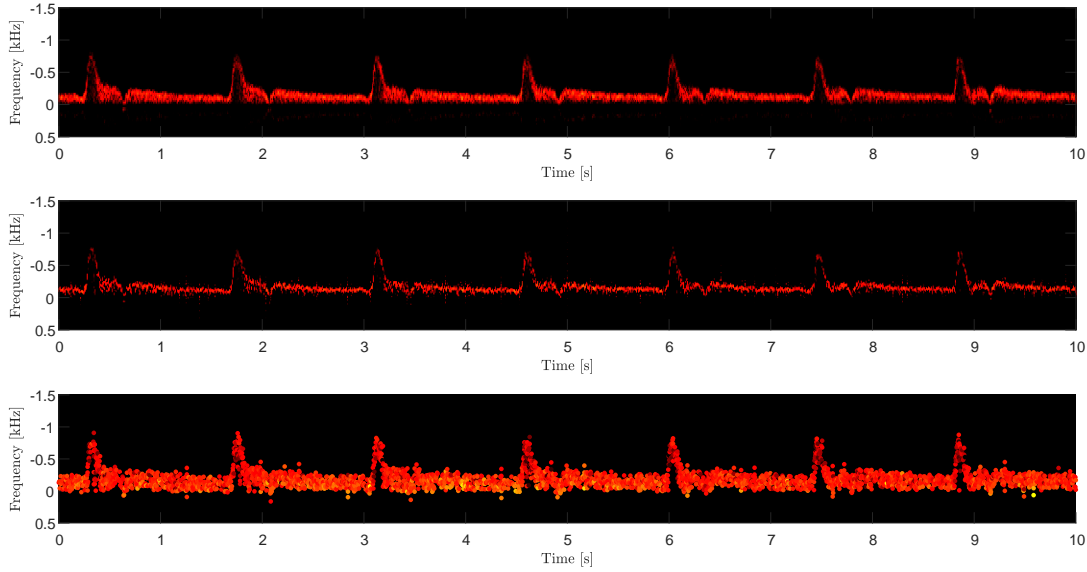
$$f(x) = x + \frac{P}{x}.$$

Fig. 9: **In vivo.** Spectrograms of in vivo data of Carotid artery. (Top) Welch's method using the fully sampled data, (middle) NEST and (bottom) NESPRIT using 35 pulses out of 128 ($\sim 27\%$) according the nested transmission pattern. All spectrograms are displayed with a dynamic range of 70 dB.

The function $f(x)$ is continuous and differentiable over the open interval $(1, \sqrt{P})$. Its derivative is given by

$$\frac{df}{dx} = 1 - \frac{P}{x^2} < 0,$$

hence, $f(x)$ is monotonically decreasing. Since $\mathcal{D}_1 \subset [1, \sqrt{P}]$, denoting $\tilde{N}_1 = \max(\mathcal{D}_1)$, we have

$$f(\tilde{N}_1) < f(d), \quad d \in \mathcal{D}_1, \ d \neq \tilde{N}_1.$$

Therefore, the optimal solution is given by $N_1 = \max(\mathcal{D}_1) - 1$ and $N_2 = \frac{P}{\tilde{N}_1} = \min(\mathcal{D}_2)$ accordingly. By interchanging the roles of $\tilde{N}_1$ and N_2 we get the solution for $\tilde{N}_1 \geq N_2$, given by $N_1 = \min(\mathcal{D}_2) - 1$ and $N_2 = \max(\mathcal{D}_1)$.

APPENDIX C
PROOF OF THEOREM 4

First, consider a given K-level nested array with L levels and $\{N_i\}_{i=1}^{L}$. Notice that if $N_K = 1$, then the resulting geometry can be seen as a nested array with $L - 1$ levels and $\{\tilde{N}_i\}_{i=1}^{L-1}$ where

$$\tilde{N}_i = N_i, \quad i = 1, ..., L - 2,$$
$$\tilde{N}_{L-1} = N_{L-1} + 1.$$

Therefore, we assume that $N_K > 1$ to avoid ambiguity.

For simplicity of analysis, we define

$$Z_i \triangleq \begin{cases} N_i + 1, & i = 1, 2, .., K - 1, \\ N_K, & i = K. \end{cases}$$

An equivalent problem to (59) can be rewritten as

$$\min_{\substack{K \in \mathbb{N}^+}} \quad \min_{\substack{Z_1, ..., Z_K \in \mathbb{N}^+ \\ Z_1, ..., Z_K \geq 2}} \quad \sum_{i=1}^{K} Z_i - K + 1 \tag{67}$$
$$\text{subject to} \quad \prod_{i=1}^{K} Z_i = P.$$

Following (67), we wish to prove that $K = \Omega$ and the optimal $\{Z_i\}_{i=1}^{\Omega}$ are given by the prime factors of P with repetitions according to their multiplicities (up to rotation).

Assume by contradiction that the optimal solution satisfies $K \neq \Omega$. The fundamental theorem of arithmetic states that every positive integer has a single unique prime factorization [60], hence, $K \leq \Omega$. Assume $K < \Omega$; then there exists Z_i which is not prime, i.e., Z_i can be decomposed into the multiplication of two smaller integers Z_{i1} and Z_{i2} where $Z_{i1}, Z_{i2} \geq 2$. This amounts to breaking the ith nested level into 2 levels such that now there are $K + 1$ levels of nesting. Assuming that $Z_{i1} \leq Z_{i2}$ without loss of generality, we have

$$Z_{i1} + Z_{i2} \leq 2Z_{i2} \leq Z_{i1}Z_{i2}. \tag{68}$$

Hence, breaking up the ith nesting level into two levels decreases the value of the objective function in contradiction to the optimality of the solution.

Following the latter, we can go on splitting the nesting levels until all Z_i are prime numbers. This, along with the fact that the prime factorization is unique, implies that the total number of levels of nesting is $K = \Omega$ and the optimal $\{Z_i\}_{i=1}^{\Omega}$ are the prime factors of P.

REFERENCES

[1] J. A. Jensen, *Estimation of blood velocities using ultrasound: A signal processing approach*. Cambridge University Press, 1996.

[2] P. Welch, "The use of fast Fourier transform for the estimation of power spectra: A method based on time averaging over short, modified periodograms," *IEEE Transactions on Audio and Electroacoustics*, vol. 15, no. 2, pp. 70–73, 1967.

[3] P. Stoica, R. L. Moses *et al.*, *Spectral Analysis of Signals*. Pearson Prentice Hall Upper Saddle River, NJ, 2005, vol. 452.

[4] K. Kristoffersen and B. A. Angelsen, "A time-shared ultrasound Doppler measurement and 2-D imaging system," *IEEE Transactions on Biomedical Engineering*, vol. 35, no. 5, pp. 285–295, 1988.

[5] H. Klebæk, J. A. Jensen, and L. K. Hansen, "Neural network for sonogram gap filling," in *International Ultrasonics Symposium*, vol. 2. IEEE, 1995, pp. 1553–1556.

[6] J. A. Jensen, "Spectral velocity estimation in ultrasound using sparse data sets," *The Journal of the Acoustical Society of America (ASA)*, vol. 120, no. 1, pp. 211–220, 2006.

[7] S. K. Mollenbach and J. A. Jensen, "Duplex scanning using sparse data sequences," in *International Ultrasonics Symposium*. IEEE, 2008, pp. 5–8.

[8] P. Liu and D. Liu, "Periodically gapped data spectral velocity estimation in medical ultrasound using spatial and temporal dimensions," in *International Conference on Acoustics, Speech and Signal Processing (ICASSP)*. IEEE, 2009, pp. 437–440.

[9] E. G. Larsson and J. Li, "Spectral analysis of periodically gapped data," *IEEE Transactions on Aerospace and Electronic Systems*, vol. 39, no. 3, pp. 1089–1097, 2003.

[10] E. Gudmundson, A. Jakobsson, J. A. Jensen, and P. Stoica, "Blood velocity estimation using ultrasound and spectral iterative adaptive approaches," *Signal Processing*, vol. 91, no. 5, pp. 1275–1283, 2011.

[11] F. Gran, A. Jakobsson, and J. A. Jensen, "Adaptive spectral Doppler estimation," *IEEE Transactions on Ultrasonics, Ferroelectrics, and Frequency Control*, vol. 56, no. 4, 2009.

[12] H. Torp, "Clutter rejection filters in color flow imaging: A theoretical approach," *IEEE Transactions on Ultrasonics, Ferroelectrics, and Frequency Control*, vol. 44, no. 2, pp. 417–424, 1997.

[13] Y. C. Eldar and G. Kutyniok, *Compressed sensing: Theory and Applications*. Cambridge University Press, 2012.

[14] S. M. Zobly and Y. M. Kakah, "Compressed sensing: Doppler ultrasound signal recovery by using non-uniform sampling & random sampling," in *28th National Radio Science Conference (NRSC)*. IEEE, 2011, pp. 1–9.

[15] S. M. Zobly and Y. M. Kadah, "Multiple measurements vectors compressed sensing for Doppler ultrasound signal reconstruction," in *International Conference on Computing, Electrical and Electronics Engineering (ICCEEE)*. IEEE, 2013, pp. 319–322.

[16] L. Demanet and L. Ying, "Wave atoms and sparsity of oscillatory patterns," *Applied and Computational Harmonic Analysis*, vol. 23, no. 3, pp. 368–387, 2007.

[17] J. Richy, D. Friboulet, A. Bernard, O. Bernard, and H. Liebgott, "Blood velocity estimation using compressive sensing," *IEEE Transactions on Medical Imaging*, vol. 32, no. 11, pp. 1979–1988, 2013.

[18] J. Richy, H. Liebgott, R. Prost, and D. Friboulet, "Blood velocity estimation using compressed sensing," in *International Ultrasonics Symposium (IUS)*. IEEE, 2011, pp. 1427–1430.

[19] O. Lorintiu, H. Liebgott, and D. Friboulet, "Compressed sensing Doppler ultrasound reconstruction using block sparse Bayesian learning," *IEEE Transactions on Medical Imaging*, vol. 35, no. 4, pp. 978–987, 2016.

[20] Z. Zhang and B. D. Rao, "Extension of SBL algorithms for the recovery of block sparse signals with intra-block correlation," *IEEE Transactions on Signal Processing*, vol. 61, no. 8, pp. 2009–2015, 2013.

[21] ——, "Recovery of block sparse signals using the framework of block sparse Bayesian learning," in *International Conference on Acoustics, Speech and Signal Processing (ICASSP)*. IEEE, 2012, pp. 3345–3348.

[22] P. Pal and P. P. Vaidyanathan, "Nested arrays: A novel approach to array processing with enhanced degrees of freedom," *IEEE Transactions on Signal Processing*, vol. 58, no. 8, pp. 4167–4181, 2010.

[23] P. Pal and P. Vaidyanathan, "A novel array structure for directions-of-arrival estimation with increased degrees of freedom," in *International Conference on Acoustics Speech and Signal Processing (ICASSP)*. IEEE, 2010, pp. 2606–2609.

[24] J. A. Jensen, "Field: A program for simulating ultrasound systems," in *10th Nordicbaltic Conference on Biomedical Imaging, vol. 4, supplement 1, part 1: 351–353*. Citeseer, 1996.

[25] J. A. Jensen and N. B. Svendsen, "Calculation of pressure fields from arbitrarily shaped, apodized, and excited ultrasound transducers," *IEEE Transactions on Ultrasonics, Ferroelectrics, and Frequency Control (UFFC)*, vol. 39, no. 2, pp. 262–267, 1992.

[26] H. L. Van Trees, *Optimum Array Processing. Part IV of Detection, Estimation, and Modulation Theory*. New York: Wiley Intersci., 2002.

[27] W.-K. Ma, T.-H. Hsieh, and C.-Y. Chi, "Doa estimation of quasi-stationary signals via Khatri-Rao subspace," in *International Conference on Acoustics, Speech and Signal Processing (ICASSP)*. IEEE, 2009, pp. 2165–2168.

[28] ——, "Doa estimation of quasi-stationary signals with less sensors than sources and unknown spatial noise covariance: A Khatri–Rao subspace approach," *IEEE Transactions on Signal Processing*, vol. 58, no. 4, pp. 2168–2180, 2010.

[29] P. Pal and P. Vaidyanathan, "Nested arrays in two dimensions, Part I: Geometrical considerations," *IEEE Transactions on Signal Processing*, vol. 60, no. 9, pp. 4694–4705, 2012.

[30] ——, "Nested arrays in two dimensions, Part II: Application in two dimensional array processing," *IEEE Transactions on Signal Processing*, vol. 60, no. 9, pp. 4706–4718, 2012.

[31] G. Montaldo, M. Tanter, J. Bercoff, N. Benech, and M. Fink, "Coherent plane-wave compounding for very high frame rate ultrasonography and transient elastography," *IEEE Transactions on Ultrasonics, Ferroelectrics, and Frequency Control*, vol. 56, no. 3, pp. 489–506, 2009.

[32] P. Pal and P. Vaidyanathan, "Soft-thresholding for spectrum sensing with coprime samplers," in *8th Sensor Array and Multichannel Signal Processing Workshop (SAM)*. IEEE, 2014, pp. 517–520.

[33] D. L. Donoho, "De-noising by soft-thresholding," *IEEE Transactions on Information Theory*, vol. 41, no. 3, pp. 613–627, 1995.

[34] A. Koochakzadeh and P. Pal, "Non-asymptotic guarantees for correlation-aware support detection," in *International Conference on Acoustics, Speech and Signal Processing (ICASSP)*. IEEE, 2018.

[35] Y. Chi, L. L. Scharf, A. Pezeshki, and A. R. Calderbank, "Sensitivity to basis mismatch in compressed sensing," *IEEE Transactions on Signal Processing*, vol. 59, no. 5, pp. 2182–2195, 2011.

[36] P. Pal and P. Vaidyanathan, "A grid-less approach to underdetermined direction of arrival estimation via low rank matrix denoising," *IEEE Signal Processing Letters*, vol. 21, no. 6, pp. 737–741, 2014.

[37] ——, "Gridless methods for underdetermined source estimation," in *48th Asilomar Conference on Signals, Systems and Computers*. IEEE, 2014, pp. 111–115.

[38] C.-L. Liu and P. Vaidyanathan, "Remarks on the spatial smoothing step in coarray MUSIC," *IEEE Signal Processing Letters*, vol. 22, no. 9, pp. 1438–1442, 2015.

[39] Y. C. Eldar, *Sampling Theory: Beyond Bandlimited Systems*. Cambridge University Press, 2015.

[40] R. Roy and T. Kailath, "Esprit-estimation of signal parameters via rotational invariance techniques," *IEEE Transactions on Acoustics, Speech, and Signal Processing*, vol. 37, no. 7, pp. 984–995, 1989.

[41] V. Y. Pan and Z. Q. Chen, "The complexity of the matrix eigenproblem," in *Proceedings of the thirty-first annual ACM symposium on Theory of computing*. ACM, 1999, pp. 507–516.

[42] G. Xu and T. Kailath, "Fast subspace decomposition," *IEEE Transactions on Signal Processing*, vol. 42, no. 3, pp. 539–551, 1994.

[43] M. A. Lediju, B. C. Byram, and G. E. Trahey, "Sources and characterization of clutter in cardiac b-mode images," in *International Ultrasonics Symposium (IUS)*. IEEE, 2009, pp. 1419–1422.

[44] W. R. Hedrick, D. L. Hykes, and D. E. Starchman, *Ultrasound Pysics and Instrumentation: Practice examinations*. CV Mosby, 1995.

[45] J. Avdal, L. Lovstakken, and H. Torp, "Effects of reverberations and clutter filtering in pulsed Doppler using sparse sequences," *IEEE Transactions on Ultrasonics, Ferroelectrics, and Frequency Control*, vol. 62, no. 5, pp. 828–838, 2015.

[46] C. Alfred and L. Lovstakken, "Eigen-based clutter filter design for ultrasound color flow imaging: a review," *IEEE Transactions on Ultrasonics, Ferroelectrics, and Frequency Control*, vol. 57, no. 5, 2010.

[47] C.-L. Liu and P. Vaidyanathan, "Super nested arrays: Sparse arrays with less mutual coupling than nested arrays," in *International Conference on Acoustics, Speech and Signal Processing (ICASSP)*. IEEE, 2016, pp. 2976–2980.

[48] ——, "Super nested arrays: Linear sparse arrays with reduced mutual coupling—Part I: Fundamentals," *IEEE Transactions on Signal Processing*, vol. 64, no. 15, pp. 3997–4012, 2016.

[49] ——, "Super nested arrays: Linear sparse arrays with reduced mutual coupling—Part II: High-order extensions," *IEEE Transactions on Signal Processing*, vol. 64, no. 16, pp. 4203–4217, 2016.

[50] ——. (2016) Super nested program. [Online]. Available: http://systems.caltech.edu/dsp/students/clliu/SuperNested/SN.zip

[51] I. S. Merrill *et al.*, "Introduction to radar systems," *Mc Grow-Hill*, 2001.

[52] P. Vaidyanathan and P. Pal, "Coprime sampling and arrays in one and multiple dimensions," in *Multiscale Signal Analysis and Modeling*. Springer, 2013, pp. 105–137.

[53] P. P. Vaidyanathan and P. Pal, "Sparse sensing with co-prime samplers and arrays," *IEEE Transactions on Signal Processing*, vol. 59, no. 2, pp. 573–586, 2011.

[54] P. Pal and P. P. Vaidyanathan, "Coprime sampling and the MUSIC algorithm," in *Digital Signal Processing Workshop and IEEE Signal Processing Education Workshop (DSP/SPE)*, 2011, pp. 289–294.

[55] P. Vaidyanathan and P. Pal, "Direct-MUSIC on sparse arrays," in *International Conference on Signal Processing and Communications (SPCOM)*. IEEE, 2012, pp. 1–5.

[56] P. Pal and P. Vaidyanathan, "Correlation-aware techniques for sparse support recovery," in *Statistical Signal Processing Workshop (SSP)*. IEEE, 2012, pp. 53–56.

[57] Z. Tan, Y. C. Eldar, and A. Nehorai, "Direction of arrival estimation using co-prime arrays: A super resolution viewpoint," *IEEE Transactions on Signal Processing*, vol. 62, no. 21, pp. 5565–5576, 2014.

[58] P. Vaidyanathan and P. Pal, "Theory of sparse coprime sensing in multiple dimensions," *IEEE Transactions on Signal Processing*, vol. 59, no. 8, pp. 3592–3608, 2011.

[59] J. R. Womersley, "Oscillatory motion of a viscous liquid in a thin-walled elastic tube—I: The linear approximation for long waves," *The London, Edinburgh, and Dublin Philosophical Magazine and Journal of Science*, vol. 46, no. 373, pp. 199–221, 1955.

[60] H. Riesel, "Prime numbers and computer methods for factoring," Royal Institute of Technology in Sweden: Birkhauser Boston 1994.